Analysis of Ni nanoparticle gas phase sintering

Sergej Tsyganov and Jochen Kästner
Experimentalphysik, Universität Duisburg-Essen, D-47048 Duisburg, Germany

Bernd Rellinghaus*
IFW Dresden, Helmholtzstr. 20, D-01069 Dresden, Germany;

Thomas Kauffeldt
Institut für Verbrennung und Gasdynamik, Universität Duisburg-Essen, D-47048 Duisburg, Germany

Frank Westerhoff and Dietrich Wolf
Theoretische Festkörperphysik, Universität Duisburg-Essen, D-47048 Duisburg, Germany
(Received 24 October 2006; published 17 January 2007)

The sintering of Ni nanoparticle agglomerates in the gas phase is studied. The partially or completely sintered agglomerates are characterized in flight by *in situ* electrical mobility measurement and after their deposition by transmission electron microscopy. The mobility diameter, the mean primary particle diameter, and the total surface area of the agglomerates are determined as functions of the sintering temperature. The experimental results are analyzed using an empirical law for the primary particle coarsening as well as by means of a modified Koch-Friedlander theory. It turns out that the activation energy for the dominating diffusion process is E_a=0.6 eV/atom, which is characteristic for surface diffusion in Ni. Our analysis provides a consistent picture with respect to both the temperature dependence of the characteristic sintering time and the mean diffusion length.

DOI: 10.1103/PhysRevB.75.045421 PACS number(s): 61.46.Df, 65.80.+n, 66.30.Pa, 81.07.−b

I. INTRODUCTION

Within the last decade, considerable scientific interest has focused on the physical properties of metallic nanoparticles because of their potential for the industrial production of materials or devices exhibiting the unique properties of nanosized structures. Among the different methods applied, the production of nanoparticles using the gas phase synthesis by inert gas condensation[1] exhibits several advantages, as, e.g., easy scalability to large production rates and high material purity. Nevertheless, this method bears some difficulties to be overcome, as, e.g., the polydispersity of the particles and their agglomeration. To provide nanoparticles with definite properties, i.e., with definite size and morphology, a heat treatment of the primary particles, subsequent to their initial coalescence and coagulation, is usually necessary. In order to control this process efficiently, a detailed knowledge of the morphological changes and the coalescence behavior of the primary particles during the sintering is highly desirable.

Theoretically, different approaches have been used so far to study the sintering of nanoparticles. Macroscopic continuum physics has been employed to describe the initial stage of sintering. Nichols and Mullins[2,3] and later Coblenz *et al.*[4] have studied the influence of different diffusion mechanisms on both the evolution of a sinter neck between adjacent particles and the characteristic sintering time. Koch and Friedlander[5] have developed a self-preserving model for the sintering by assuming the minimization of the agglomerate surface as the essential driving force for the sintering process. Based upon these studies, models for the mutual interplay between interparticle coalescence on the one side and coagulation (i.e., the successive formation of agglomerates) on the other side have been developed.[6–11]

More recently, molecular dynamics and kinetic Monte Carlo simulations have been employed to microscopically investigate the coalescence behavior of faceted (i.e., thermodynamically equilibrated, nonspherical) metallic nanoparticles[12–15] as well as the complete evolution process of nanoparticles in the gas phase.[16,17]

Experimentally, the sintering behavior of nanoparticles in the gas phase has been studied for both metals and nonmetals (see, e.g., Refs. 6–10 and references therein). The variation of the particle number concentration, the primary particle diameter, the effective agglomerate size, and the agglomerate morphology with time and temperature constitute the central aspects of these investigations. Little is, however, available on the experimental determination of the relevant activation energies for the gas phase sintering, although this property is in general well suited to distinguish between the various sintering mechanisms. The reliable determination of this activation energy is one of the main foci of the present work.

One important experimental quantity for the analysis and description of the gas phase sintering is the electrical mobility of the agglomerate or particle which is related to its size. The mobility change during sintering is measured *in situ* by means of differential electrical mobility analyzers (DMA). The agglomerate or particle morphology, however, cannot be directly inferred from DMA measurements, since the mobility diameter as the measured quantity refers only to the true geometric diameter if the agglomerate or particle is compact and spherical-like. Hence, another experimental method, namely transmission electron microscopy (TEM) is necessary and suitable to provide complementary information about the change of the agglomerate morphology, especially in the early stage of sintering, when the agglomerates exhibit

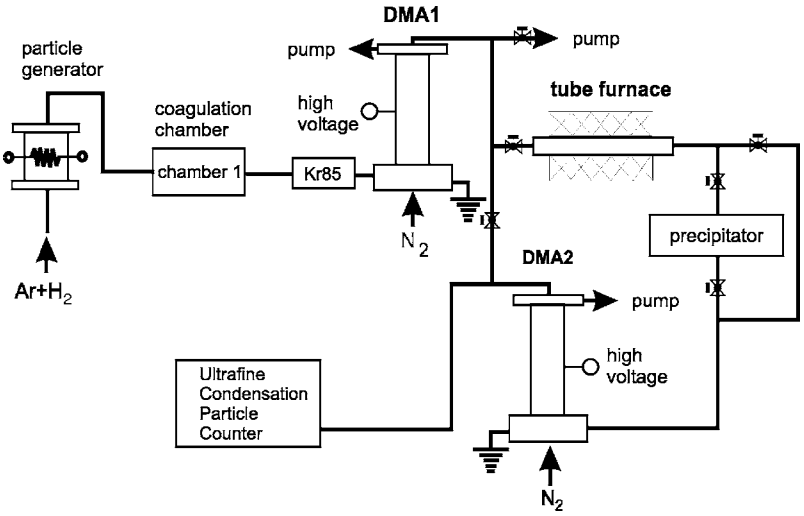

FIG. 1. Schematic drawing of the experimental setup for the gas phase preparation of Ni nanoparticles.

fractal-like morphologies. In addition, TEM provides the possibility to measure the primary particle size and the surface areas of particles or particle agglomerates.

In this paper, the sintering behavior of Ni nanoparticles is studied by both DMA measurements and TEM investigations. Previous studies on Ni particles were mainly focused on the investigation of oxidic shells on the sintering behavior[18,19] or were bound for relatively large primary particles with sizes beyond 25 nm.[20] The present experiments are conducted in reducing atmosphere and provide numbers for the agglomerate mobility diameter, for the primary particle diameter, and for the agglomerate surface area as function of the sintering temperature. The results are compared with macroscopic sintering theories. Using a modified Koch-Friedlander model, we show that the sintering is consistently described by dominant surface diffusion of the coalescent Ni particles.

II. EXPERIMENT

The experimental setup for the generation and gas phase sintering of the Ni nanoparticles is schematically shown in Fig. 1. High-purity Ar (99.999%) with a 2% addition of hydrogen is used as a carrier gas for the particles. Here, the hydrogen content serves as a reducing agent to avoid particle oxidation due to residual oxygen. The carrier gas is continuously flowing at a pressure of 1013 mbar and a flow rate of 1.6 l/min throughout the whole experimental setup. Nickel is evaporated into the gas flow from a high-purity Ni wire (99.995%) which is electrically heated to 1260(±1%) °C. The Ni particles nucleate from the supersaturated vapor and subsequently coagulate mainly in the coagulation chamber (volume 2.2l) within a time interval of 1 to 2 min.

Having passed a radioactive ^{85}Kr charger, the polydisperse agglomerates carry predominantly a single electron charge. They are fractionated with respect to their electrical mobility by a first differential mobility analyzer (DMA1).[21,22] In such a differential mobility analyzer (DMA), the aerosol (i.e., the carrier gas and the particle agglomerates) is passing a cylindrical capacitor. Within the electrical field of the capacitor, the charged agglomerates experience a transverse electrical force resulting in a transverse drift velocity proportional to this force. The proportionality factor is the so-called electrical mobility, which is a function of charge, mass, and shape of the particles. A variation of the electrical field thus allows to fractionate the particles, which may escape the capacitor through a lateral aperture, with respect to their electrical mobility. The mobility equivalent diameter of an arbitrarily shaped particle (or particle agglomerate), D_M, is defined as the diameter of a compact, spherical particle with the same electrical mobility. Thus, although d_M is always related to the geometric size of the particle, only for spherical particles are the two diameters identical (for details, see Refs. 21 and 22).

In our experiment, monodisperse agglomerates with a mobility diameter of $d_M=60\pm6$ nm are extracted from the polydisperse agglomerates ($\overline{d_M}=25.7$ nm, geometrical standard deviation $\sigma_G=1.97$). The selection of such a relatively large mobility diameter allows to study the sinter process of a sufficiently large number (~100) of agglomerated primary particles.

After this size selection, the agglomerates are carried through a tube furnace which is rather uniformly heated to sintering temperatures T_S between 23 °C and 1000 °C. The residence time of the particles within the furnace, i.e., the time during which the particles are subjected to the sintering temperature, is kept constant at $t=7$ s for all particles under investigation. Subsequently, the sintered particle agglomerates are either electrostatically deposited in a precipitator onto amorphous carbon film substrates for *ex situ* electron microscopy investigations or conducted to a second DMA (DMA2) to determine their mobility diameter after sintering *in situ*. After having passed DMA1 and/or DMA2 the particles are counted using an ultrafine condensation particle counter.

A Philips CM12 microscope (LaB_6, 120 keV) has been used for TEM. From TEM investigations on deposited particles, the particle size, morphology, crystal structure, and surface area have been determined after sintering at different temperatures T_S. Especially, the diameter d_P of the coagulated primary particles and the surface area A of the agglomerates are determined by means of TEM.

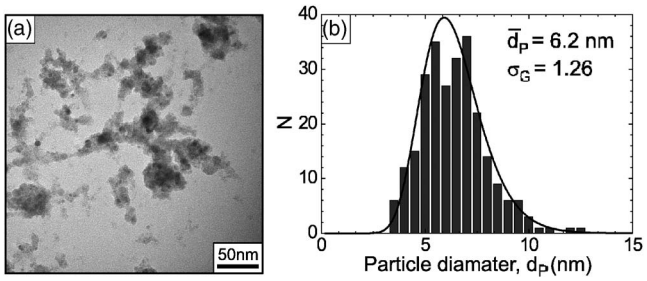

FIG. 2. (a) TEM micrograph of primary Ni particles deposited on amorphous carbon film immediately behind the particle generator. (b) Size distribution of unsintered primary particles. The solid line is a log-normal fit to the experimental data. d_P and σ_G denote the mean particle diameter and the geometrical standard deviation.

III. RESULTS AND DISCUSSION

Figure 2(a) shows a typical TEM micrograph of Ni primary particles deposited and agglomerated on a carbon film immediately behind the exit of the particle generator, i.e., before entering the coagulation chamber. In Fig. 2(b), the size distribution of the diameter d_P of the primary particles, as measured on several TEM micrographs obtained at very high magnifications, is shown. The distribution exhibits a log-normal behavior with a mean diameter $\bar{d}_P$=6.2 nm and a geometrical standard deviation of σ_G=1.26. This result is typical for all our investigated Ni particles. It represents the primary coalescence conditions of the particles in the particle generator and was proved to be rather independent of the carrier gas composition, and it does not depend on the hydrogen concentration. Electron diffraction shows that the unsintered Ni primary particles are fcc polycrystals with grain sizes of 1 to 2 nm. The lattice constant is determined to be a=0.36±0.01 nm, which is slightly larger than the bulk value of a_0=0.3524 nm.

Figure 3(a) presents a TEM micrograph of two Ni particle agglomerates deposited after having passed the coagulation chamber, the size selector (DMA1, d_M=60 nm) and the tube furnace at room temperature (RT). The schematic drawing in Fig. 3(b) illustrates the meaning of the diameters d_M and d_P. The figure shows agglomerates of only weakly sintered primary particles, exhibiting a fractal-like morphology with small voids between the particles. Electron diffraction patterns obtained from such RT-sintered agglomerates exhibit a low contrast and show only blurred diffraction fringes [Fig. 3(c)] thus indicating a low degree of crystallinity.

Figure 4 shows a series of TEM micrographs of particle agglomerates which have been sintered at temperatures in the range 23 °C≤T_S≤800 °C. It is worthwhile noting here that at low sintering temperatures, T_S<250 °C, the overall size of the agglomerates is only slightly reduced with increasing T_S, while the diameter d_P of the primary particles continuously grows at the expense of the particle number within individual agglomerates. Concurrently, some of the voids are growing whereas others are vanishing. In the temperature range 250 °C<T_S<300 °C, a drastic change of the agglomerate morphology is observed: The few remaining voids open, i.e., particles which are multiply connected at lower T_S become singly connected at elevated sintering temperatures.

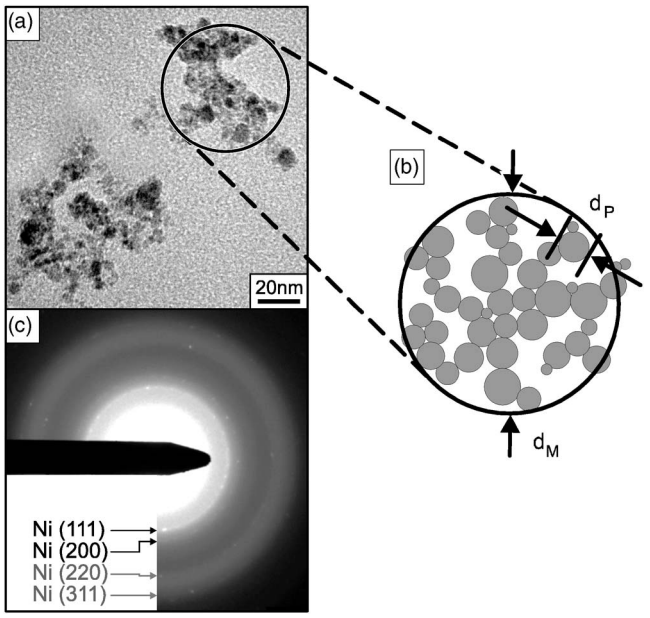

FIG. 3. (a) TEM micrograph of two particle agglomerates with mobility diameter d_M=60 nm sintered at room temperature. (b) Schematic illustration of the agglomerate mobility diameter d_M and the primary particle diameter d_P. (c) Electron diffraction pattern of the sample.

Further increase of the sintering temperature results in the growth of some grains while the sinter neck size approaches the size of neighboring grains. Here, the primary particle diameter d_P refers to the grain size. At T_S=500 °C, the agglomerates are sintered to single particles, consisting of only a few grains, distinguishable in the TEM images due to diffraction contrast. At T_S>500 °C, the particles become increasingly spherically shaped whereas the number of grains does not essentially change. Here the primary particle diameter d_P, i.e., the mean grain size is almost as large as the diameter of the whole particle. At about 800 °C, the particles approach thermal equilibrium which is indicated by the occurrence of facets at the particle surfaces. Increasing T_S further up to 1000 °C does not result in any particular change of the particle size or shape.

Throughout the whole series of TEM micrographs presented in Fig. 4, it can be seen from the diffraction contrast (i.e., the dark areas within the particles or agglomerates) that the grain size successively increases with increasing T_S. However, even at T_S=800 °C the particles are not single crystals but are rather sub-divided into smaller grains.

Figure 5 shows both the mobility diameter d_M as determined *in situ* with DMA2 and the diameter d_P of the primary particles as determined from TEM images as functions of the sintering temperature T_S. Here, d_P represents the median of a log-normal distribution function fitted to the experimentally determined sizes, and the error bars are the standard deviation of the according normal distribution. At first glance, the temperature dependencies of d_M and d_P appear similar, except for their sign. However, there is a sudden decrease of d_M within the narrow temperature interval between 250 and 300 °C; before at higher sintering temperatures, the decrease of d_M levels off and finally approaches the diameter of the fully sintered particles of roughly 30 nm.

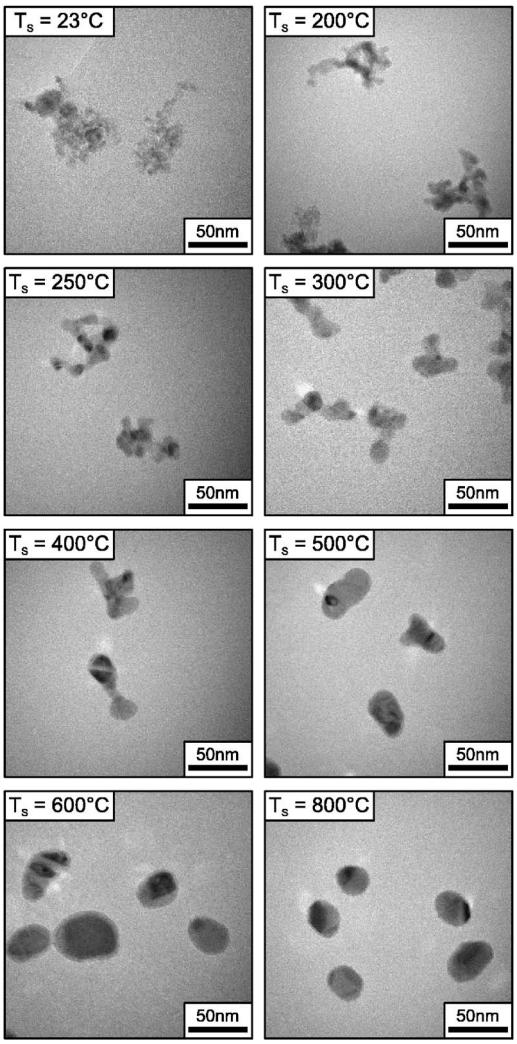

FIG. 4. Series of micrographs of Ni nanoparticles deposited on carbon films after gas phase sintering for $t=7$ s at different temperatures T_S as indicated on the images.

Strikingly, the temperature range of the sudden drop in d_M coincides exactly with the temperature for which the TEM images indicate the occurrence of a major morphological change due to the opening or vanishing of voids within the

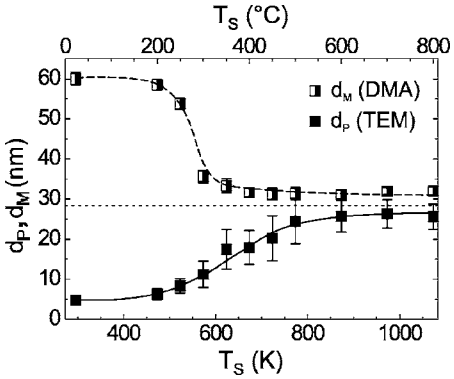

FIG. 5. Mobility diameter d_M and primary particle diameter d_P vs sintering temperature T_S as determined *in situ* with DMA and *ex situ* from TEM, respectively. Lines are guides to the eye.

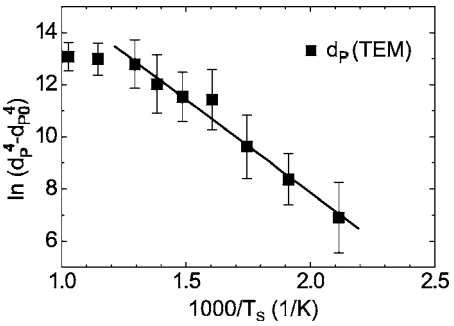

FIG. 6. Arrhenius plot for primary particle diameters as determined from TEM images. The straight line represents a least square fit to the data for 200 °C $\leq T_S \leq$ 500 °C.

particle agglomerates (s.a.). Since the voids are smaller than the mean free path of the carrier gas atoms [$\lambda(N_2) \simeq 70$ nm], they are "invisible" to the DMA. The measured mobility diameter d_M is therefore larger than that of an agglomerate with similar structure but without voids. Furthermore, the increase of the void dimensions observed at low sintering temperatures may in part compensate for the compaction of the agglomerates as evidenced by the increase of d_P with increasing T_S. The growth of the primary particle diameter d_P with increasing T_S is rather continuous, the steepest increase of d_P occurring at sintering temperatures from 300 to 400 °C before at higher T_S, d_P approaches a value of about 26 nm. This mean grain diameter is only slightly smaller than the mean diameter d_M of the fully sintered agglomerates.

In order to characterize the gas phase sintering process quantitatively, the initial growth of the primary particles can be analyzed according to an empirical relation derived for the grain growth during thermal sintering in nanocrystalline materials:[8]

$$d_P^N(T_S) - d_{P0}^N = C_1 \cdot D_0 \cdot t \cdot e^{-E_a/k_B T_S}. \quad (1)$$

Here d_P and d_{P0} denote the final and the initial diameter of the particles (i.e., after and before sintering), C_1 a proportionality constant, t the time of the particle exposure to the sintering (Kelvin) temperature T_S, D_0 the pre-exponential factor of the diffusion constant, E_a the activation energy for the relevant diffusion process, and k_B the Boltzmann constant. The exponent N is somewhat uncertain and discussed in the literature to vary between 2 and 4, depending on the sintering model employed. $N=2$ can be derived from an evaporation-condensation model; $N=4$ is adequate for a surface or grain boundary diffusion process. According to Eq. (1), the activation energy of the diffusion process relevant for the gas phase sintering of Ni nanoparticles can be determined from Arrhenius plots for $d_P^N - d_{P0}^N$. A plot, using $N=4$, is shown in Fig. 6. Linear regression of the experimental data up to 500 °C gives $E_a = 0.61 \pm 0.1$ eV/atom. From an Arrhenius plot, using $N=2$ (not shown), $E_a = 0.37 \pm 0.1$ eV/atom is derived. We note here that Eq. (1) does not allow for a description of the saturation effect of the particle growth due to the finite size of the agglomerates (see Fig. 5), which is also seen in Fig. 6 at the two highest temperatures.

TABLE I. Diffusion constants for nickel as taken from the literature. D_0, E_a, and T are the pre-exponential factor of the diffusion constant, the activation energy, and the temperature interval of the measurement, respectively. Abbreviations: Vol = volume diffusion. GB = grain boundary diffusion. $S(hkl)[h'k'l']$=surface diffusion on an (hkl) plane in $[h'k'l']$ direction. FIM = field ion microscopy. P=powder sample. PC =polycrystal. SC=single crystal. TF=thin film. [$^{\alpha}$pure Ni, $^{\beta}$ commercial grade Ni (Ref. 34)]

Diffusion path	D_0 (m^2/s)	E_a (kJ/mol)	E_a (eV/at.)	T (K)	Grain size (sample)	Ref.
Vol	1.9×10^{-4}	279.5	2.90	475–650	(SC)	23
Vol	1.33×10^{-4}	280.8	2.91	606–920	(SC)	24
GB	-	46	0.48	20–200	70 nm (P)	25
GB	-	102	1.06	227–427	100–400 nm (P)	26
GB	-	116	1.20	270–650	500 nm (TF)	27
GB	-	170	1.76	300–600	4 μm (TF)	27
GB	4.4×10^{-11}	187	1.94	368–1051	70 μm (PC)	28
GB	7×10^{-6}	114.6	1.19	475–650	30–70 μm (PC)	23
GB	-	276	2.86	850–1000	110 μm (PC)	29
S	-	90	0.93	237–477	(FIM tip)	30
S(110)[$1\bar{1}0$]	9×10^{-7}	73	0.76	500–877	(SC)	31
S(110)[001]	4.7×10^{-2}	188.3	1.95	500–877	(SC)	31
S(111)	3×10^{-2}	159	1.65	614–840		32
S(110)	1×10^{-6}	52	0.54	625–935		33
S	8×10^{-8}	75	0.78	800–1200	150 μm^{α} (PC)	34
S	1.8×10^{-7}	89	0.92	800–1200	150 μm^{β} (PC)	34
S(110)	2×10^{-6}	85	0.88	800–1080	(SC)	35

Comparison with literature data for the diffusion constants of Ni as collected in Table I reveals the following: The activation energy for the gas phase sintering of Ni nanoparticles is significantly smaller than data reported for volume diffusion. For $N=4$, E_a is comparable with activation energies associated with surface diffusion. For Ni nanoparticles, however, a clear distinction between surface and grain boundary diffusion is difficult, since the grain boundary diffusion constant, as taken from the literature data, decreases with grain size and may become as small as that for surface diffusion. Moreover, the important pre-exponential factor D_0 of the diffusion constant cannot be determined using the empirical relation, Eq. (1), since the constant C_1 is unknown.

An alternative method to determine the parameters characterizing the dominant diffusion process for the sintering of Ni nanoparticles is based on the determination of the agglomerate surface area $A(T_S)$. Experimentally, A can be determined either from the measured mobility diameter, $A=A_{\mathrm{DMA}}$, or from TEM micrographs, $A=A_{\mathrm{TEM}}$. Since the DMA is not capable to determine the agglomerate morphology, A_{DMA} can only be calculated with the crude assumption that the agglomerate is dense and spherical, i.e., $A_{\mathrm{DMA}}=\pi d_M^2$. This assumption is justified for agglomerate structures, as obtained at high sintering temperatures where d_P and d_M are comparably large.

For the determination of A_{TEM}, we use two geometric approximations illustrated in Fig. 7. At low sintering temperatures ($T_S<300$ °C) the deposited agglomerates mostly consist of "flat" and loosely interconnected branches of primary particles. Here we apply the "holey pancake" geometry approximation, where $A_{\mathrm{TEM}}=2A_{\mathrm{proj}}+ld_P$, with $2A_{\mathrm{proj}}$ being the up and down side projection area, l and d_P being the length and width of the circumference area, respectively, including inner circumference areas due to voids. A_{proj}, l, and d_P are determined from TEM micrographs of a series of agglomerates at each sintering temperature. At high sintering temperatures ($T_S>300$ °C), the spherical geometry is applied, thus $A_{\mathrm{TEM}}=4A_{\mathrm{proj}}$. At temperatures near $T_S=300$ °C, both approximations give essentially the same result for A.

In Fig. 8, the surface areas A_{DMA} and A_{TEM} are plotted as a function of the sintering temperature T_S. Both areas decrease with increasing T_S. Coinciding above 300 °C, they approach at high sintering temperatures the surface area of a solid sphere with about 30 nm diameter. At low T_S, A_{DMA} is significantly larger than A_{TEM}. This is ascribed to the fact that in A_{TEM}, the fractal-like morphology and the occurrence of

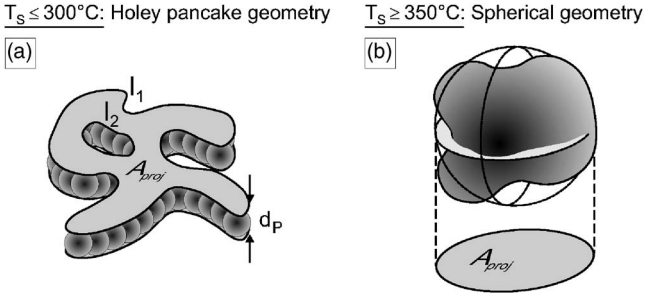

FIG. 7. Schematic illustration of approximations used for the temperature-dependent determination of the Ni particle agglomerate surface areas from TEM micrographs.

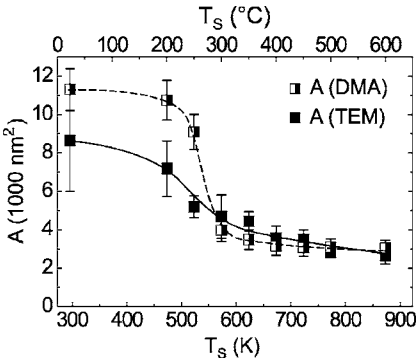

FIG. 8. Sintering temperature dependence of Ni nanoparticle surface areas A as determined from DMA measurements and TEM investigations. Lines are guides to the eye.

voids is taken into account which is not the case for A_{DMA}. On the other hand, the image contrast of the particles is quite weak at low T_S, causing a relatively large error in A_{TEM}.

The quantitative analysis of the $A(T_S)$ data is based on the phenomenological model of Koch and Friedlander.[5] Within this model, the driving force for thermal sintering is the minimization of the surface free energy which necessitates a reduction of the agglomerate surface area, the rate of which is assumed to behave as

$$\frac{dA}{dt} = -\frac{1}{\tau_S}(A - A_{eq}). \tag{2}$$

Here, τ_S and A_{eq} are the characteristic sintering time and the surface area of the thermally equilibrated, i.e., fully sintered agglomerate, respectively. From macroscopic continuum theories of sintering via surface diffusion, the sintering time τ_S is predicted to vary with the fourth power of the particle size:[2,3]

$$\tau_S = CR^4 \quad \text{with } C = \frac{k_B T_S}{25 D \gamma a^4}, \tag{3}$$

where R, D, γ, and a are the radius of the primary particles within the agglomerates, the diffusion constant, the surface free energy, and the atomic diameter, respectively. If the solid particles are not amorphous, the surface free energy is not constant, but rather a function of the surface orientation. Nevertheless, Eq. (3) remains valid with some effective value of γ, provided all surfaces are above their roughening temperature. Then the sintering process leads to an equilibrium shape which is rounded everywhere, but is not a sphere. Lowering the temperature to below the roughening temperature of the low index surfaces leads at first to isolated facets in these directions, completely surrounded by parts that are still rough. Upon further decreasing the temperature, surfaces with higher indices also cease to be rough until at $T=0$ the crystal is completely faceted. Recent Monte Carlo simulations[14] have shown that faceted elongated particles assume their more isotropic equilibrium shape more slowly than expected from Eq. (3), because crystal growth on the facets requires the nucleation of new islands. This is slow. Hence, the continuum theory of mass transport leading to Eq. (3) is only valid for the rounded surface parts which are still above their roughening temperature. This raises the question whether Eq. (3) is applicable for the sinter temperatures considered in our experiments. We claim it is, because when the coagulated primary particles enter the sintering furnace they are most likely not faceted, even for temperatures below the roughening temperature for low index surfaces. The reason is that they form during a rapid thermal quench in the cold carrier gas when leaving the nucleation zone. Thus, the particle agglomerates entering the sintering furnace are far from being thermally equilibrated. They have a low degree of crystallinity as confirmed by electron diffraction [see Fig. 3(c)]. Moreover, no facets were observed in the TEM images in this case. Consequently, no facets inhibit the initial stages of sintering when the sintering furnace is switched on. Although particles, which are subjected to sintering temperature of about 400 °C, have developed small facets, they still have large rounded surface areas. Therefore, we may assume that the sinter interval is short enough that the sinter process is *not* affected by the need to nucleate islands on terraces, which means that for our experimental situation, Eq. (3) remains valid.

To solve Eqs. (2) and (3), we make the simplifying assumption that each agglomerate consists of $\nu(R)$ identical spherical particles with radius R. From our experimental observations we can deduce that the total volume V, i.e., the total mass of the agglomerate, is conserved during the sintering process:

$$V = \nu(R)\frac{4\pi}{3}R^3 = \text{const} = \frac{4\pi}{3}R_{eq}^3, \tag{4}$$

where R_{eq} is the radius of the fully sintered, i.e., the spherical particle. This leads to a temperature-dependent rescaling of the surface area A with $\nu(R)$:

$$A = \nu(R)4\pi R^2, \tag{5}$$

and it follows that

$$R = 3\frac{V}{A}. \tag{6}$$

With Eqs. (3) and (6), the Koch-Friedlander equation [Eq. (2)] can be rewritten as

$$\frac{dA}{dt} \approx -\frac{A^4}{C(3V)^4}(A - A_{eq}). \tag{7}$$

The implicit solution of this equation is

$$t = CR_{eq}^4 f(A), \tag{8}$$

where $f(A)$ is a function solely dependent on the agglomerate surface area before sintering, A_0, during sintering, A, and in the fully sintered state, A_{eq}:

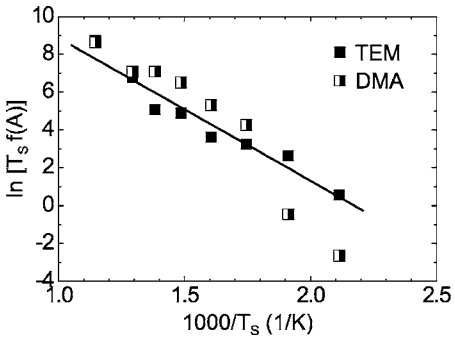

FIG. 9. Arrhenius plot according to Eq. (10) with surface area data A, determined from DMA and TEM measurements, respectively. Error bars, amounting to roughly ±1 on a ln scale, are omitted for clarity. Solid line represents least square fit to the TEM data.

$$f(A) = \ln\left|\frac{1-\frac{A_{eq}}{A_0}}{1-\frac{A_{eq}}{A}}\right| - \frac{A_{eq}}{A_0}\left(\frac{A_0}{A}-1\right) - \frac{1}{2}\left(\frac{A_{eq}}{A_0}\right)^2\left[\left(\frac{A_0}{A}\right)^2-1\right] - \frac{1}{3}\left(\frac{A_{eq}}{A_0}\right)^3\left[\left(\frac{A_0}{A}\right)^3-1\right]. \quad (9)$$

With $D=D_0\exp(-E_a/k_BT_S)$, it follows from Eqs. (3) and (8) that

$$T_S \cdot f(A) = \frac{25\gamma a^4 D_0 t}{k_B R_{eq}^4} \cdot e^{-E_a/k_BT_S} = \Gamma \cdot e^{-E_a/k_BT_S}. \quad (10)$$

Using the experimental A_{TEM} and A_{DMA} data as temperature-dependent surface areas $A(T_S)$, both the activation energy E_a of the diffusion constant and the pre-exponential factor D_0 can be determined from an Arrhenius plot $\ln[T_S f(A)]$ vs $1/T_S$. The resulting plots are shown in Fig. 9. As one can see, good agreement is achieved between the data of A_{TEM} and A_{DMA} except for $T_S<300$ °C $(1000/T_S>1.8)$, where A_{DMA} is likely to be enhanced with respect to the "real" agglomerate surface area due to the occurrence of voids. From linear regressions of both the TEM data and the DMA data above 250 °C, activation energies of $E_a=0.65\pm0.1$ eV/atom and $E_a=0.60\pm0.1$ eV/atom are obtained, respectively. Using the surface free energy for Ni of $\gamma=2$ J/m^2,[36] the according pre-exponential factors are determined to be $D_0=1\times10^{-11}$ m^2/s and $D_0=8\times10^{-12}$ m^2/s, respectively. Together with E_a and D_0 as obtained from the temperature-dependent primary particle diameter $d_P(T_S)$ (Fig. 6), these results are collected in Table II.

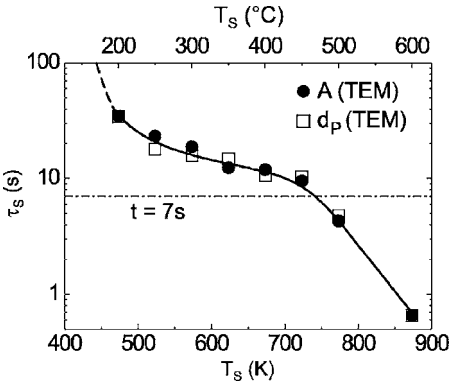

FIG. 10. Characteristic sintering time $\tau_S(T_S)$ as calculated from surface area data A and $A(d_P)$, determined with TEM, according to Eqs. (6) and (11). Uncertainty of τ_S amounts roughly to a factor of 2. The solid line is a guide to the eye, the dashed dotted straight line represents the experimental sintering time $t=7$ s.

Using Eqs. (3), (6), (8), and (9), the characteristic sintering time $\tau_S(T_S)$ is determined from both the experimental $A_{\mathrm{TEM}}(T_S)$ and $d_P(T_S)$ data:

$$\tau_S = \frac{t}{f(A)} \cdot \left(\frac{A_{eq}}{A}\right)^4 = \frac{t}{f(A(d_P))} \cdot \left(\frac{d_P}{d_{P,eq}}\right)^4. \quad (11)$$

The results are shown in Fig. 10. $\tau_S(T_S)$, as calculated from these two nearly independently determined sets of experimental data, agree very well. As expected, τ_S decreases rapidly with increasing sintering temperature T_S due to the increase of the diffusion constant D. The temperature range 250 °C$<T_S<$450 °C, where the slope of $\log(\tau_S)$ vs T_S is smaller than at lower and higher temperatures, defines the sintering range. Here, the decrease of τ_S is slowed down by the increase of R^4 due to the particle coarsening [see Eq. (3)]. Above $T_S\simeq450$ °C, the sintering process of the Ni nanoparticles is essentially completed, since at these temperatures, τ_S becomes equal to or smaller than the experimental sintering time of $t=7$ s. This finding is in excellent agreement with the temperature dependence of d_P and d_M (cf. Fig. 5), and thus corroborates our thermal analysis.

TABLE II. Activation energies E_a and pre-exponential factors D_0 for the gas phase sintering of Ni nanoparticles as derived from *in situ* DMA and *ex situ* TEM investigations. The uncertainties in E_a amount to ±10 kJ/mol or ±0.1 eV/atom, respectively

No.	Method of analysis	D_0 (m^2/s)	E_a (kJ/mol)	E_a (eV/at.)	T (°C)	Remarks
1	$d_P(T)$–TEM	-	36±10	0.37±0.1	200–500	Empirical, $N=2$
2	$d_P(T)$–TEM	-	59±10	0.61±0.1	200–500	Empirical, $N=4$
3	$A_S(T)$–TEM	1×10^{-11}	63±10	0.65±0.1	200–600	mod. KF model
4	$A_S(T)$–DMA	8×10^{-12}	58±10	0.60±0.1	300–600	mod. KF model
	Avg. (2–4)	$\mathbf{9\times10^{-12}}$	60±10	0.62±0.1	**200–600**	-

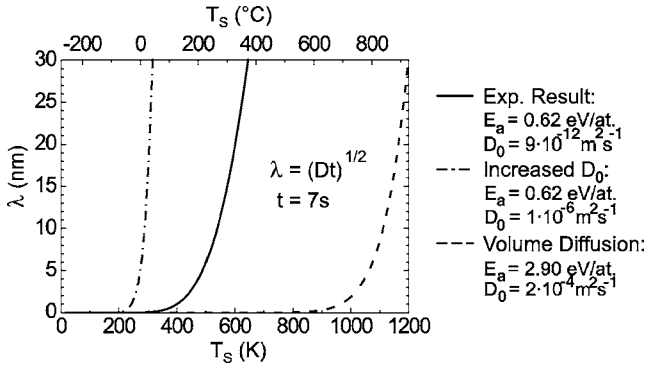

FIG. 11. Diffusion length λ vs sintering temperature T_S. Solid line as calculated from experimental result, dashed-dotted line as calculated with significant increase of pre-exponential factor D_0, and dashed line as calculated from the volume self-diffusion constant for Ni.

Further confirmation arises from an investigation of the mean diffusion length λ. The temperature dependence of this characteristic length can be estimated from the diffusion constant and the experimental sintering time according to $\lambda = \sqrt{Dt}$. As presented in Fig. 11, the resulting $\lambda(T_S)$ curve (solid line) covers the range of experimentally observed primary particle sizes ($5\ \text{nm} \leq d_P \leq 30\ \text{nm}$) exactly in that temperature interval ($200\ ^\circ\text{C} \leq T_S \leq 450\ ^\circ\text{C}$), where substantial particle growth occurs. A significantly increased pre-exponential factor D_0 (dash-dotted line) would lead to a situation where sintering is completed (i.e., $d_P \simeq 30$ nm) already at lower temperatures. On the other hand, increasing the activation energy to a value of $E_a = 2.9$ eV/atom as associated with volume diffusion in bulk Ni,[23,24] results in a delayed onset of diffusion on length scales large enough to account for the observed primary particle sizes.

IV. SUMMARY

We have studied the sintering behavior of size-selected Ni nanoparticle agglomerates for a fixed sintering time and different sintering temperatures T_S between 23 °C and 800 °C. DMA measurements of the electrical mobility diameter d_M show a pronounced decrease with increasing T_S in a narrow temperature interval. As TEM investigations reveal, this decrease of d_M is accompanied by a major change of the agglomerate morphology, namely, the opening of agglomerate voids and the transition from a fractal to a spherical-like shape. Measurement of the growth of the primary particle diameter d_P by TEM show, however, a more graduate increase with increasing T_S. The agglomerate surface areas A_{TEM} and A_{DMA}, as determined independently from TEM and DMA measurements, exhibit a similar temperature dependence for T_S above 300 °C. Below 300 °C, A_{DMA} is substantially larger than A_{TEM}, which is probably due to the voids, seen in the fractal-like agglomerates at low sintering temperatures. Using an empirical relation for the temperature dependence of the primary particle growth and a modified Koch-Friedlander model for the temperature dependence of the agglomerate surface reduction, we determine in both cases essentially the same activation energy for the dominating diffusion process for the sintering, $E_a = 0.62$ eV/atom. As becomes obvious from a comparison with the diffusion data on Ni available in the literature, this value is characteristic for the surface diffusion of Ni. The analysis further provides a consistent picture of the sintering process, when comparison is made, on the one hand, between the experimental sintering time t and the calculated characteristic sintering time $\tau_S(T_S)$, and on the other hand, between the diffusion length $\lambda(D,t)$ and the diameters d_M and d_P of the fully sintered agglomerate.

ACKNOWLEDGMENTS

This work is supported by the Deutsche Forschungsgemeinschaft within Sonderforschungsbereich 445.

*Electronic address: B.Rellinghaus@ifw-dresden.de

[1] R. Birringer, H. Gleiter, H. P. Klein, and P. Marquardt, Phys. Lett. **102A**, 365 (1984).
[2] F. A. Nichols and W. W. Mullins, J. Appl. Phys. **36**, 1826 (1965).
[3] F. A. Nichols, J. Appl. Phys. **37**, 2805 (1966).
[4] W. S. Coblenz, J. M. Dynys, R. M. Cannon, and R. L. Coble, Mater. Sci. Res. **13**, 141 (1980).
[5] W. Koch and S. K. Friedlander, J. Colloid Interface Sci. **140**, 419 (1990).
[6] F. E. Kruis, K. A. Kusters, and S. E. Pratsinis, Aerosol Sci. Technol. **19**, 514 (1993).
[7] T. Seto, M. Shimada, and K. Okuyama, Aerosol Sci. Technol. **23**, 183 (1995).
[8] *Nanomaterials: Synthesis, Properties and Applications*, edited by A. S. Edelstein and R. C. Cammarata (Institute of Physics, London, UK, 1996), p. 182.
[9] S. Tsantilis and S. E. Pratsinis, AIChE J. **46**, 407 (2000).
[10] See e.g., K. Nakaso, M. Shimada, K. Okuyama, and K. Deppert, Aerosol Sci. Technol. **33**, 1061 (2002), and references therein.
[11] R. C. Flagan and M. M. Lunden, Mater. Sci. Eng., A **204**, 113 (1995).
[12] H. Zhu and R. S. Averback, Philos. Mag. Lett. **73**, 27 (1996).
[13] L. J. Lewis, P. Jensen, and J. L. Barrat, Phys. Rev. B **56**, 2248 (1990).
[14] N. Combe, P. Jensen, and A. Pimpinelli, Phys. Rev. Lett. **85**, 110 (2000).
[15] S. Hendy, S. A. Brown, and M. Hyslop, Phys. Rev. B **68**, 241403 (2003).
[16] M. Zachariah and M. J. Carrier, J. Aerosol Sci. **30**, 1139 (1999), and references therein.
[17] R. Meyer, J. J. Gafner, S. L. Gafner, S. Stappert, B. Rellinghaus, and P. Entel, Phase Transitions **78**, 35 (2005).
[18] Y. Sakka and T. Uchikoshi, Powder Metall. **36**, 179 (1993).
[19] S. A. Sethi and A. R. Thölén, Nanostruct. Mater. **4**, 903 (1994).

[20] A. V. Ragulya and V. V. Skorokhod, Nanostruct. Mater. **5**, 835 (1995).
[21] F. Stratmann, Th. Kauffeldt, D. Hummes, and H. Fissan, Aerosol Sci. Technol. **26**, 368 (1997).
[22] W. C. Hinds, *Aerosol Technology* (Wiley, New York, 1999).
[23] A. R. Wazzan, J. Appl. Phys. **36**, 3596 (1965).
[24] K. Maier, H. Mehrer, E. Lessmann, and W. Schle, Phys. Status Solidi B **78**, 689 (1976).
[25] B. Bokstein, H. Bröse, L. Trusov, and T. Khvostantseva, Nanostruct. Mater. **6**, 873 (1995).
[26] A. P. Zhilyaev, G. V. Nurislamova, S. Suriñach, M. D. Baró, and T. G. Langdon, Mater. Phys. Mech. **5**, 23 (2002).
[27] J. Spingarn, B. Jacobson, and W. Nix, Thin Solid Films **45**, 507 (1977).
[28] P. Neuhaus and C. Herzig, Z. Metallkd. **79**, 595 (1988).
[29] S. Karashima, H. Oikawa, and T. Motomiya, Trans. Jpn. Inst. Met. **10**, 205 (1969).
[30] A. J. Melmed, J. Appl. Phys. **38**, 1885 (1961).
[31] H. Bonzel and E. Latta, Surf. Sci. **76**, 275 (1978).
[32] J. Wolfe and H. Waert, in *The Structure and Chemistry of Solid Surfaces*, edited by G. Somorjai (Wiley, New York, 1969), p. 32.
[33] A. Graham, W. Silvestri, and J. Toennies, *Surface Diffusion in Atomistic and Collective Processes*, edited by M. Tringides (Plenum, New York, 1997).
[34] J. Blakely and H. Mykura, Acta Metall. **9**, 23 (1961).
[35] H. Bonzel and N. Gjostein, J. Appl. Phys. **39**, 3480 (1968).
[36] *Handbook of Chemistry and Physics*, edited by R. C. Weast (CRC Press, West Palm Beach, Fl, 1978–1979), p. F-33.